



42 infiltration and can bypass soil-matrix pores to reach deeper soil layers (Bachmair et al., 2012; Franklin et al., 2021).
43 Preferential flow intensity and morphology vary markedly among vegetation types. Woodland slopes are
44 characterized by deep, continuous macropore channels, predominantly vertical preferential flow, rapid infiltration,
45 and greater deep-soil water storage (Niu et al., 2023; Cai et al., 2024; Zhang et al., 2025). Shrubland slopes exhibit
46 predominantly lateral and diffuse subsurface flow with weak vertical components, thereby retaining much of the
47 infiltrating water in shallow soil layers (Wang et al., 2020; An et al., 2022; Liang et al., 2023; Zhang et al., 2024).
48 Herbaceous slopes rely mainly on surface cracks and earthworm burrows to route water, and therefore preferential
49 flow channels are sparse and discontinuous (Wen et al., 2020; Niu et al., 2023; Li et al., 2025). Vegetation recovery
50 has significantly restructured the soil bio-pore system through root penetration, thereby facilitating the development
51 of preferential-flow pathways and making infiltration regimes more heterogeneous (Zhao et al., 2022; Guan et al.,
52 2024). However, preferential-flow infiltration on steep slopes, particularly at landslide sites with different vegetation
53 types, has not been adequately investigated. During heavy storms, preferential flow can regulate spatiotemporal
54 subsurface water dynamics and act as a biologically mediated control on slope stability.

55 Root morphology and spatial configuration influence rainwater infiltration pathways and soil moisture
56 redistribution (Fan et al., 2020; Li et al., 2023). On the Chinese Loess Plateau, two predominant vegetation types are
57 recognized: woodlands dominated by *Robinia pseudoacacia* and *Pinus tabulaeformis*, and shrublands dominated by
58 *Rosa xanthina* and *Hippophae rhamnoides*. Woodland trees typically develop deeply penetrating root systems,
59 forming continuous macropore networks and vertical preferential-flow pathways (Zhao et al., 2022; Cai et al., 2024;
60 Wang and Zhang, 2024). These structures facilitate rapid rainfall infiltration into deep soil layers, enhance subsurface
61 moisture retention, delay surface saturation, and reduce surface runoff (Souza et al., 2023; Cai et al., 2024; Hu et al.,
62 2025). In contrast, shrubs develop a dense, fibrous root matrix that promotes mesopores and capillaries formation,
63 thereby accelerating the formation of subsurface saturation zones and limiting vertical percolation (Laycock et al.,
64 1967; Souza et al., 2023; Xiao et al., 2024; Yamase et al., 2024). Therefore, plant roots can control preferential-flow
65 patterns and alter hillslope hydrology. However, few studies have examined how the hydrological effects of mature
66 vegetation influence landslides on the Chinese Loess Plateau.

67 To examine hydrological and mechanical heterogeneity in mature woodland and shrubland stands on steep
68 slopes and its implications for slope stability, we first analyze landslide geometry and landscape dissection for slides
69 triggered by a low-intensity storm from 3 to 6 October 2021. Then, we assess hydrological heterogeneity in mature
70 woodland and shrubland using soil-moisture observations, excess soil-water ratios across different soil-water storage
71 levels, and preferential-flow pathway identification. Mechanical heterogeneity is characterized by soil and root
72 strength parameters, the soil water characteristic curve (SWCC), and the hydraulic conductivity function (HCF).
73 Finally, we evaluate slope failure potential in relation to landslide density in the two stands. This study mainly
74 addresses the role of vegetation in modulating slope stability by analyzing real landslide cases. Our findings highlight
75 the dual role of vegetation in mitigating landslide erosion and provide new insights into its nuanced effects on
76 hillslope stability.

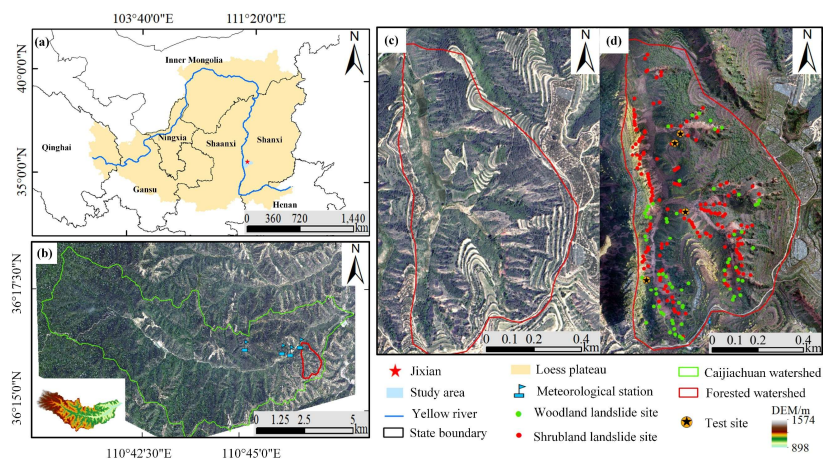
77 2. Research background

78 2.1 Study area

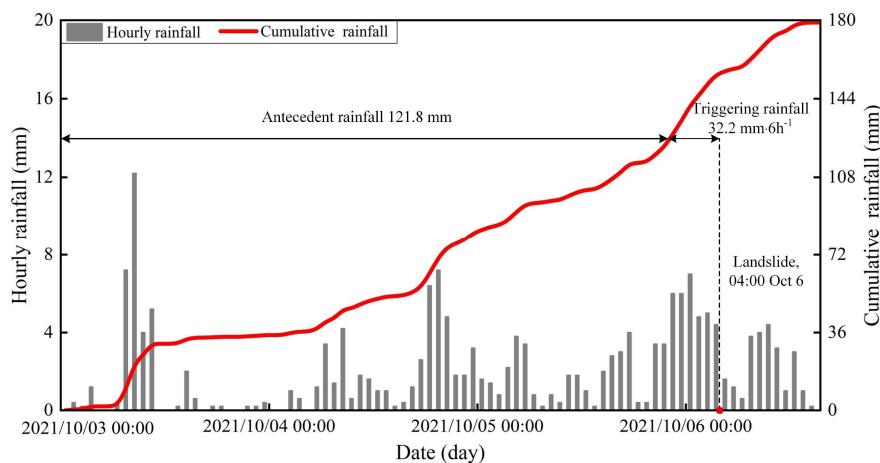
79 The study area lies in a forested catchment on the southeastern Loess Plateau in China (Fig. 1a). It is located in
80 the downstream reach of the Caijiachuan watershed in Jixian County, Shanxi Province (Fig. 1b). The soil has an
81 unconsolidated, porous structure. On steep slopes, woodland is dominated by *Robinia pseudoacacia* and shrubland
82 by *Rosa xanthina*. Since the farmland reforestation policy was implemented in 1980, forest cover has recovered to
83 about 70%. During 1990–1995 and 1999–2002, the Mountain Improvement Technology Training Project enhanced



84 forest regeneration. Currently, the local soil and water conservation measures serve as a benchmark within the Loess
 85 Plateau region. The study area lies in the transition zone between semi-humid and semi-arid climates, with a mean
 86 annual temperature of 9.9°C and a mean annual precipitation of 579.1 mm. Most rainfall occurs from June to
 87 September, accounting for more than 70% of the annual precipitation. Prior to the 2021 event, a short-duration storm
 88 on 25–26 August 2003 triggered 18 landslides, with antecedent precipitation of 71.7 mm over 18 hours and an
 89 intense 3 h rainfall of 24.4 mm (Wang et al., 2024). In contrast, the 2021 rainfall event was a low-intensity storm
 90 with prolonged antecedent precipitation of 121.8 mm over 72 hours and a 6 h peak rainfall of 32.2 mm (Fig. 2).
 91 After the storm, post-storm documentation mainly focused on differences in landslide numbers, densities, slope
 92 aspects, and morphological metrics (Tang et al., 2023), while giving little attention to the hydrological and
 93 mechanical conditions of landslides in the two forested land types.



94
 95 **Figure 1.** Geographical setting of the study area, with the (a) location of Caijiachuan watershed in the Loess Plateau,
 96 China, (b) the forested catchment and meteorological stations in downstream reach of Caijiachuan watershed, (c)
 97 0.15 m resolution orthoimage on 12 October 2019, and (d) 0.10 m resolution orthoimage on 14 October 2021
 98 showing the sites for soil-moisture observations and dye-tracer experiments.



99
 100

Figure 2. Hourly and cumulative rainfall from 3 to 6 October 2021.



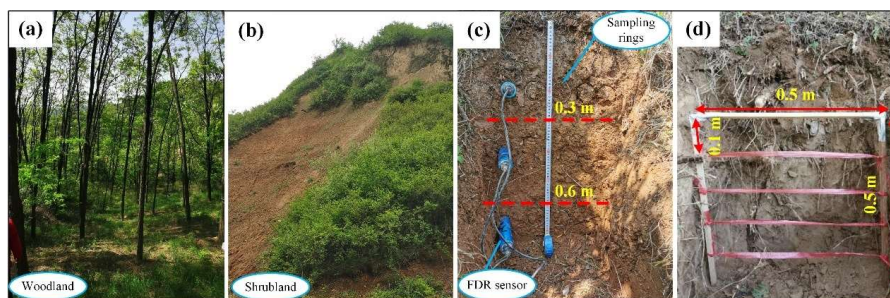
101 **3 Materials and methods**

102 **3.1 Landslide information interpretation**

103 To obtain landslide inventories for the woodland and shrubland, we acquired high-resolution orthoimages and
104 digital elevation models (DEMs) using an unmanned aerial vehicle (UAV; DJI Inspire 2). Two systematic UAV
105 flights with consistent flight and image overlap settings were conducted on 12 October 2019 (Fig. 1c) and 14 October
106 2021 (Fig. 1d). Pix4D software was used to generate ortho-mosaics and DEMs. These DEMs have spatial resolutions
107 of 0.15 m and 0.10 m, respectively, thereby supporting accurate landslide mapping. Landslide point and areal
108 densities are calculated by dividing the total number of landslides and the total scar area by the respective woodland
109 and shrubland areas, respectively. The lateral extent of each landslide is the sum of the sidewall and head scarp areas.
110 The unit upslope contribution area is the ratio of the total contributing area to the scar width. Landslide gradients
111 and associated unit contributing areas are computed from the DEM generated on 14 October 2021.

112 **3.2 Rainfall, soil moisture monitoring and sample collection**

113 In the study area, the woodland has an open structure due to sparse to moderate tree density and high canopy
114 height (Fig. 3a), whereas the shrubland has a closed structure because of high density and low canopy height (Fig.
115 3b). Both land types have a well-developed herbaceous layer. To investigate the hillslope hydrology, we used
116 frequency-domain reflectometry (FDR) soil-moisture sensors installed at depths of 30, 60, and 90 cm to record
117 volumetric water content from May to August 2023 (Fig. 3c). A meteorological station at Caijiachuan Forest Station
118 is located about 2 km from the study area. Both soil moisture and rainfall were recorded at 5-min intervals. During
119 soil moisture sensor installation, we collected undisturbed soil samples near the FDR sensor locations. Bulk density,
120 porosity, effective cohesion, internal friction angle, and unsaturated hydraulic properties were determined using an
121 electronic balance, an oven, a GDS triaxial apparatus, and transient release and imbibition tests (Lu and Godt, 2013).
122 Plant roots were collected to determine depth-dependent root distribution (Fig. 3d), root diameter, root area ratio,
123 and tensile strength (Nimmo et al., 2009).



124 **Figure 3.** Soil moisture monitoring and soil and root sampling. (a) Open woodland dominated by *Robinia*
125 *pseudoacacia*. (b) Close-structure shrubland dominated by *Rosa xanthina*. (c) Trench wall showing soil sampling
126 and FDR sensor installation. (d) In situ root counting and sampling at 0.1 m depth intervals.

128 **3.3 Excessive soil water due to preferential flow**

129 Previous studies of preferential flow on the Loess Plateau have shown that continuous channels in woodland
130 enhance deep soil water storage, whereas lateral and dispersed channels in shrubland keep water in shallow soil
131 layers (Wang et al., 2019; An et al., 2022). Therefore, differences in preferential-flow pathways can result in distinct
132 soil moisture responses during the same rainfall event. In this study, we first characterized preferential-flow
133 pathways using dye tracer experiments and then examined soil moisture responses using observed soil moisture data
134 in the two land types.



135 Dye tracer experiments were conducted on vegetated slopes near the soil moisture monitoring sites to examine
 136 the preferential flow pathways (Fig. 1d). An electric sprayer was used to spray a $4 \text{ g}\cdot\text{L}^{-1}$ brilliant blue solution onto
 137 a $100 \text{ cm} \times 100 \text{ cm}$ plot (Figs. 4a and 4b). After spraying the solution, the plot was immediately covered with a
 138 rainproof cloth to minimize evaporation. After 24 h, a 5 cm-wide margin of soil was removed from the plot edges,
 139 and the core area was excavated to obtain 10 vertical profiles. Excavation grids were established at 0.1 m intervals
 140 in both the longitudinal and transverse directions (Figs. 4c and 4d). Profile images were captured with a digital
 141 camera at a fixed distance and with a parallel orientation, and subsequently processed using Photoshop CS and
 142 Image-Pro Plus. The proportion of flow marked by the dye is/was quantified as:

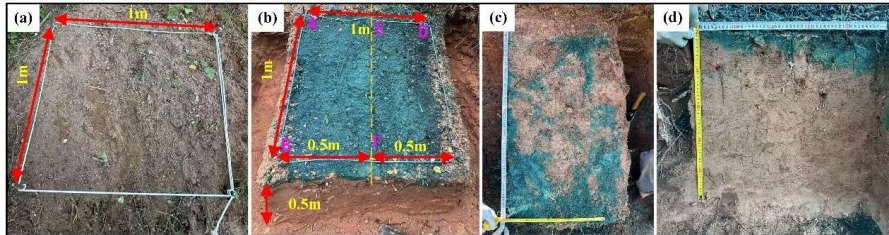
$$143 \quad SAR = \frac{a_j}{A_j} \quad (1)$$

144 where SAR is the stained-area ratio for the soil profile, j is soil depth (cm), a is the number of stained pixels at
 145 depth j , and A is the total number of pixels along the image width at depth j .

146 The soil moisture response index describes excess soil water in response to a given rainfall input:

$$147 \quad R_C = \frac{R_{max} - (R + R_0)}{R + R_0} \quad (2)$$

148 where R_C is the excess soil-water ratio in response to a given rainfall event, R_{max} is the maximum total soil-water
 149 storage during the rainfall episode (mm), R is the cumulative rainfall during the episode (mm), and R_0 is the initial
 150 total soil-water storage before the rainfall episode (mm). Positive or negative values of R_C indicates whether the
 151 increase in soil-water storage exceeds or falls below the rainfall input. In addition, R_C reflects the preferential-flow
 152 component aligned with slope orientation or gravity. As soil moisture typically lags rainfall, we follow the method
 153 proposed by Lu et al. (Lu et al., 2024), which defines rainfall episodes using soil depth and in situ saturated hydraulic
 154 conductivity measurements. Therefore, the R_C values under different $R + R_0$ conditions, together with the
 155 preferential-flow pathways, can reflect heterogeneity in soil-water movement in the woodland and shrubland.



156
 157 **Figure 4.** Dye tracer experiments and preferential flow pathways examination. (a) Experimental plot after vegetation
 158 removal. (b) Experimental plot after 24 h of brilliant blue solution spraying. (c) Horizontal dye-stained profile. (d)
 159 Transverse dye-stained profile.

160 3.4 Slope resistance to failure probability at given rainfall input

161 Hillslope resistance to failure at a given rainfall input depends on the topography and the physical, strength,
 162 and hydraulic properties of soil mass. A widely used combination of the infinite-slope stability model and a
 163 hydrological model yield an expression for the critical drainage area per unit contour length (Montgomery and
 164 Dietrich, 1994):

$$165 \quad a_{cr} = \frac{zK \sin \theta \cos \theta}{R_t} \left[\frac{C' + C_r}{\rho_w g z \cos^2 \theta \tan \phi} + \frac{\rho_s}{\rho_w} \left(1 - \frac{\tan \theta}{\tan \phi} \right) \right] \quad (3)$$

166 where a_{cr} is the critical drainage area per unit contour length ($\text{m}^2\cdot\text{m}^{-1}$), R_t is the triggering rainfall rate ($\text{m}\cdot\text{d}^{-1}$),
 167 K is the saturated hydraulic conductivity ($\text{m}\cdot\text{d}^{-1}$), θ is the slope angle ($^\circ$), C' and C_r are the effective soil



168 cohesion and root cohesion (kPa), ρ_s and ρ_w are the unit weights of soil and water ($\text{KN}\cdot\text{m}^{-3}$), z is the soil
169 thickness (m), and φ is the effective internal friction angle ($^\circ$).

170 The left-hand side of Eq. (3) represents the topographic condition of a given landslide or a site susceptible to
171 slope failure (Montgomery et al., 2000). Moving to the R left-hand side yields the right-hand side of Eq. (4) in an
172 integrated form involving only soil mass parameters:

$$173 \quad a_{cr} \times R_t = \frac{K \tan \theta (C_r + C_s)}{\rho_w g \tan \varphi} + z K \sin \theta \cos \theta \frac{\rho_s}{\rho_w} \left(1 - \frac{\tan \theta}{\tan \varphi}\right) \quad (4)$$

174 The physical meaning of $a_{cr} \times R_t$ is that hillslope resistance to failure under site-specific topographic conditions
175 and a given rainfall input strongly depends on soil physical properties. For the rain-induced loessal landslides in the
176 study area, the strength and hydraulic properties of the landslide mass in woodland and shrubland may lead to
177 different $a_{cr} \times R_t$ levels, so that landslide density (or number) differs between woodland and shrubland. Therefore,
178 we focus on $a_{cr} \times R_t$ from the right-hand side of Eq. (4) to elucidate the initiation of loessal landslides in two
179 forested land types.

180 4 Results

181 4.1 Landslides in the two lands

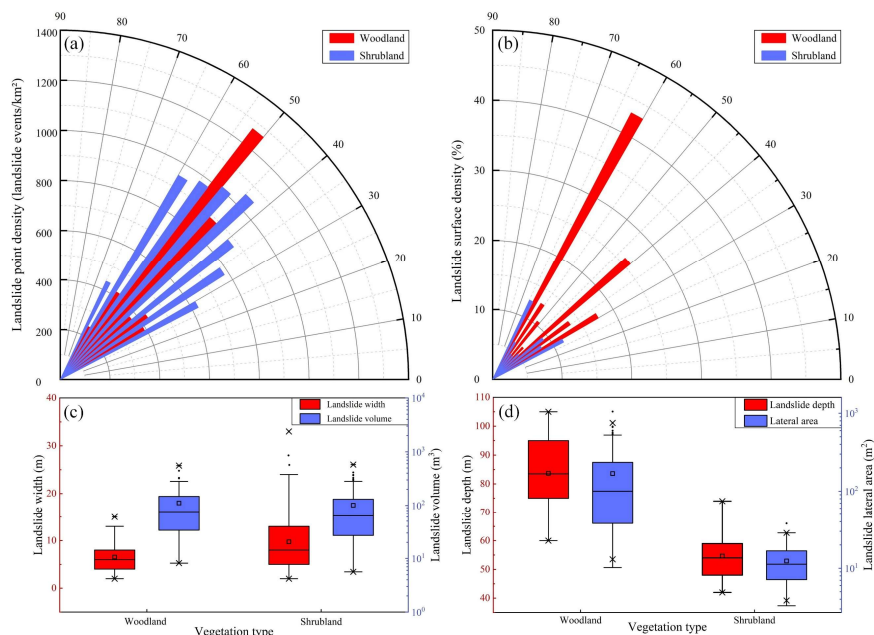
182 To compare the landslide point and areal densities between the two stands, we calculated landslide counts and
183 areas and divided them by the total steep-terrain area in each stand. This approach excluded non-susceptible terrain
184 from the analysis. The spatial distribution and morphology of landslides in woodland and shrubland exhibited clear
185 patterns. Specifically, the statistical results showed that landslide point density in shrubland was 1.56 times that in
186 woodland, whereas landslide areal density was only 0.48 times that in woodland (Figs. 5a and 5b). Furthermore, the
187 average landslide width in shrubland was 1.49 times that in woodland. Generally, trees in woodlands have deep root
188 systems that provide stronger anchoring and can mobilize deeper soil layers, thereby modifying the failure depth
189 and geometry of shallow landslides (Schwarz et al., 2010; Masi et al., 2023; Dibiagio et al., 2024). The average
190 landslide depth in woodland was 1.82 times that in shrubland, while the average lateral extent was 1.61 times that in
191 shrubland. However, the average width of landslides in woodland was only 0.67 times that in shrubland. Overall,
192 the total landslide volume in woodland was 1.16 times that in shrubland, indicating that landslides in woodland tend
193 to be larger (Figs. 5c and 5d).

194 When landslides are considered alongside other landscape-dissection agents such as rills and gullies, their
195 spatial locations depend on two controls. One is spatial competition between the slope-dependent term $S = \tan \theta$ ($\text{m}\cdot\text{m}^{-1}$)
196 and the area-dependent term A ($\text{m}^2\cdot\text{m}^{-1}$); the other is exceedance of the A - S topographic threshold (Montgomery
197 and Dietrich, 1994). As highlighted in Sect. 3.4, variations in $a_{cr} \times R_t$ arise from the interplay of topography, failure
198 depth, soil strength, plant root reinforcement, and hydraulic conductivity. To evaluate these controls on landslides,
199 we compared the upslope contributing area (A) and slope gradient (S) between the two land types.

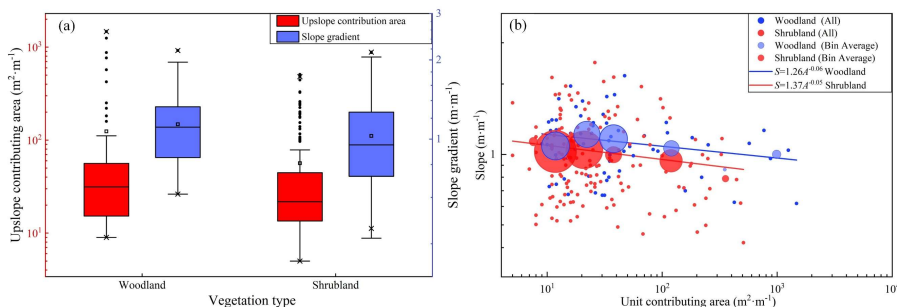
200 Field investigations reveal that most landslides in the study area occur in concave topographic positions.
201 Statistical analysis indicates that, on average, woodland sites have a significantly larger upslope contributing area
202 ($124 \text{ m}^2 \text{ m}^{-1}$) and steeper slopes (48°) than shrubland sites. These values are consistent with expectations from the
203 A - S threshold framework (Fig. 6a). Fitting regression lines to the bin-averaged dataset further demonstrates that
204 landslides in woodland generally require either a larger upslope contributing area or a steeper slope gradient for
205 initiation (Fig. 6b). The A - S relationship shows that, at similar slope gradients, landslides in woodland require larger
206 upslope contributing areas than those in shrubland. This suggests that, compared with landslides in shrubland, those
207 in woodland may require higher rainfall-intensity thresholds, steeper slopes, or both, for initiation. As a result,
208 landslide point density in woodland is about 50% lower than in shrubland under similar conditions.



209



210
 211 **Figure 5.** Landslide characteristics in woodland and shrubland. **(a)** point density by slope-gradient class; **(b)** areal
 212 density by slope-gradient class; **(c)** landslide depth and lateral area; and **(d)** landslide width and volume. The three
 213 crossing lines of box show decreasing order of 75th quantile (Q_3), median (Q_2), and 25th quantile (Q_1). The box
 214 length is the interquartile range ($IQR=Q_3-Q_1$). The small square is the average value. The upper and lower limit of
 215 whiskers are $Q_3+1.5IQR$ and $Q_1-1.5IQR$, respectively. The whiskers extend to the minimum and maximum values,
 216 except for mild outliers, which are shown as black dots.



217
 218 **Figure 6.** Upslope contributing area and slope gradient condition. **(a)** upslope contributing area and mean slope as
 219 a function of slope aspect; **(b)** upslope-contributing area vs. mean slope gradient above the landslide area. The
 220 definition of the whiskers is given in the caption of Fig. 5. Circles indicate mean slopes, with radius proportional to
 221 the number of landslides. A power-law regression is fitted to the bin-averaged data.

222 4.2 Soil Hydrological properties

223 4.2.1 SWCC and HCF curves



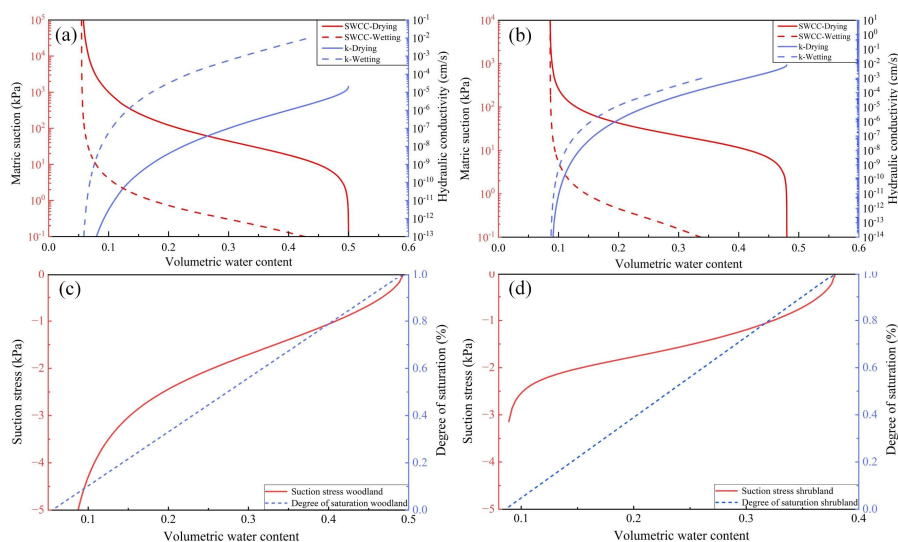
224 Extensive research has examined saturated hydraulic conductivity and microstructural properties of loess (Xu
 225 et al., 2021; Li et al., 2023). Given that loess on hillslopes largely remains unsaturated during natural rainfall
 226 infiltration and drainage (Lan et al., 2021; Wei et al., 2022), evaluating unsaturated hydro-mechanical differences
 227 using SWCCs and HCFs is important. Therefore, this approach enables comparison among key parameters—
 228 hydraulic conductivity, matric suction, suction stress, and microstructural properties.

229 Table 1 lists the soil parameters obtained through Hydrus-1D inversion. Based on these parameters, the SWCC
 230 and HCF were plotted for the woodland and shrubland sliding-layer soils (Fig. 7). The results indicate that the pore-
 231 size distribution parameter and saturated hydraulic conductivity are significantly higher for woodland soils than for
 232 shrubland soils. This contrast is evident in both drying and wetting processes. This suggests that the pore system in
 233 woodland soils is dominated by larger pores, which enhance water movement. This pore structure facilitates rainfall
 234 infiltration into the soil. In contrast, shrubland soils contain more micropores that retain more water. This is reflected
 235 in a 3.1% higher residual water content in shrubland soils than in woodland soils. During the drying test, the air-
 236 entry pressures of woodland and shrubland soils are nearly identical. However, during the wetting process, the air-
 237 entry pressure in woodland soils is 0.05 kPa lower than in shrubland soils. This indicates that larger pores in
 238 woodland soils begin to drain and fill with air at lower matric suction. As a result, at the same matric suction, a
 239 continuous gas-phase pathway forms earlier in woodland soils (Figs. 7c and 7d). This promotes air-water exchange
 240 and moisture release, making it less likely for the soil to reach or maintain a high degree of saturation for extended
 241 periods. Therefore, under the same rainfall conditions, shrubland soils have weaker moisture-buffering capacity than
 242 woodland soils, making the soil more prone to becoming highly saturated. This reduces the effective stress and shear
 243 strength of shrubland soils, ultimately reducing slope stability.

244 During the drying and wetting processes, the difference in saturated water content in shrubland sliding-layer
 245 soil (0.101) is approximately 14.43 times that in woodland sliding-layer soil (0.007). This indicates that the pore
 246 structure in shrubland sliding-layer soil is less stable than in woodland sliding-layer soil. Under extreme drying-
 247 wetting conditions, some pores tend to collapse or rearrange, making it difficult for the soil to maintain its original
 248 pore configuration. The resulting changes in pore structure disrupt water flow paths in shrubland sliding-layer soil,
 249 reducing permeability, weakening water flow, and slowing drainage. These findings are consistent with the stronger
 250 hysteresis observed in the SWCC of shrubland sliding-layer soil compared with that of woodland sliding-layer soil
 251 (Fig. 7a and 7b). They further confirm that woodland sliding-layer soil has a greater capacity for moisture
 252 redistribution.

253 **Table 1.** Parameters describing the soil and water characteristic curve (SWCC) and the hydraulic conductivity
 254 function (HCF) from Hydrus 1D

Parameters	Definition	Woodland	Shrubland
θ_s^d	Saturated moisture	0.500	0.480
θ_s^w		0.493	0.379
θ_r	Residual moisture	0.055	0.086
n^d	The pore size distribution parameter	1.58	2.19
n^w		1.69	1.88
α^d (KPa ⁻¹)	The inverse of the air entry pressure head	5.461×10^{-3}	6.294×10^{-3}
α^w (KPa ⁻¹)		0.646	0.596
K_s^d (cm·s ⁻¹)	Saturated hydraulic conductivity	2.3×10^{-5}	5.4×10^{-6}
K_s^w (cm·s ⁻¹)		7.1×10^{-2}	5.0×10^{-3}

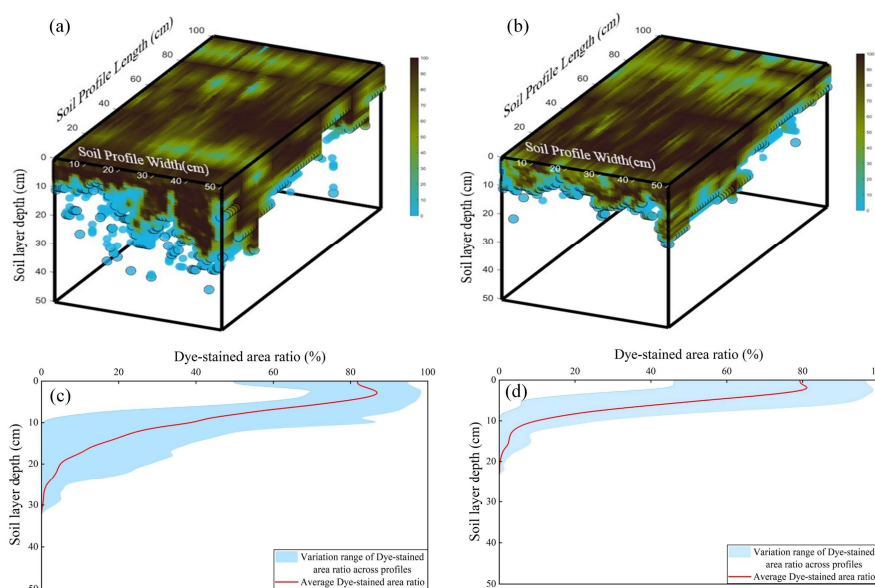


255
256 **Figure 7.** Differences in the hydromechanical properties of the sliding-layer soil. **(a)** SWCC for layer 3 of the
257 woodland soil profile; **(b)** SWCC for layer 2 of the shrubland soil profile; **(c)** Suction stress–volumetric water content
258 curves for layer 3 of the woodland soil profile; **(d)** Suction stress–volumetric water content curves for layer 2 of the
259 shrubland soil profile.

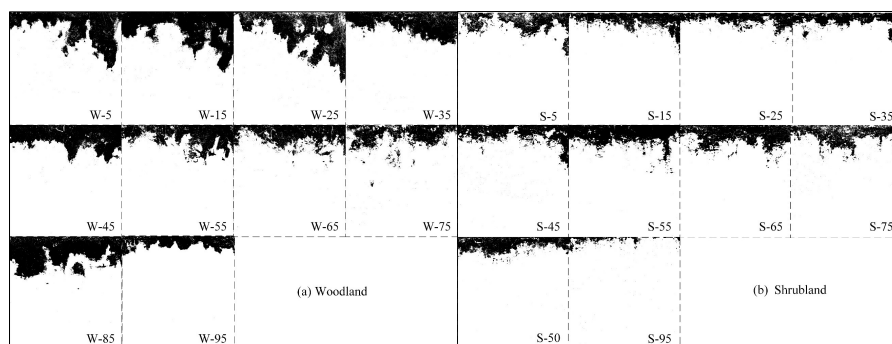
260 4.2.2 Dye tracer experiments

261 Dye-tracer experiments directly visualize the flow pathways of water infiltration in woodland and shrubland
262 soils. Under the same applied water volume and infiltration area, the stained soil volume in woodland soils is
263 markedly larger than that in shrubland soils. Three-dimensional visualizations reveal that stained pathways in
264 woodland soils form thick bands with numerous vertically continuous columnar channels. Hydraulic connectivity is
265 high, and water infiltrates to greater depths. Stained bands in shrubland soils are shallow, and vertical, filament-like
266 channels are nearly absent. In addition, the depth-dependent pattern of dye-stained area ratios in the shrubland profile
267 further confirms that vertical infiltration is restricted to relatively shallow depths. Differences in the volume, depth,
268 and morphology of the stained pathways indicate that infiltration in woodland soils no longer follows uniform
269 matrix-flow conditions. This is also evident in the dye-stained areas of vertical profiles. Woodland profiles show
270 large, continuous color patches, whereas shrubland profiles mainly show fragmented spots concentrated in shallow
271 soil. This pattern suggests that deeper shrubland soils are denser and have lower pore connectivity.

272 Overall, woodland soils more readily develop a stable, efficient vertical percolation system with greater
273 infiltration depth and stronger connectivity. This promotes deep water storage and redistribution. In contrast,
274 insufficient pore connectivity in shrubland soils causes water to remain in shallow layers, prolonging surface wetness
275 and slowing pore-water pressure recovery. Under intense rainfall, this condition favors saturation buildup and thus
276 increases the likelihood of landslide initiation. This flow pattern is consistent with differences soil-matrix hydraulic
277 behavior differences inferred from SWCC and HCF and provides a path-based complement to traditional hydraulic
278 parameters.



279
 280 **Figure 8.** Morphological characteristics of dye-stained flow paths in woodland and shrubland soils. **(a)** Three-
 281 dimensional visualization of stained zones in woodland; **(b)** Three-dimensional visualization of stained zones in
 282 shrubland; **(c)** Dye-stained area ratio vs. soil depth in woodland; **(d)** Dye-stained area ratio vs. soil depth in shrubland.



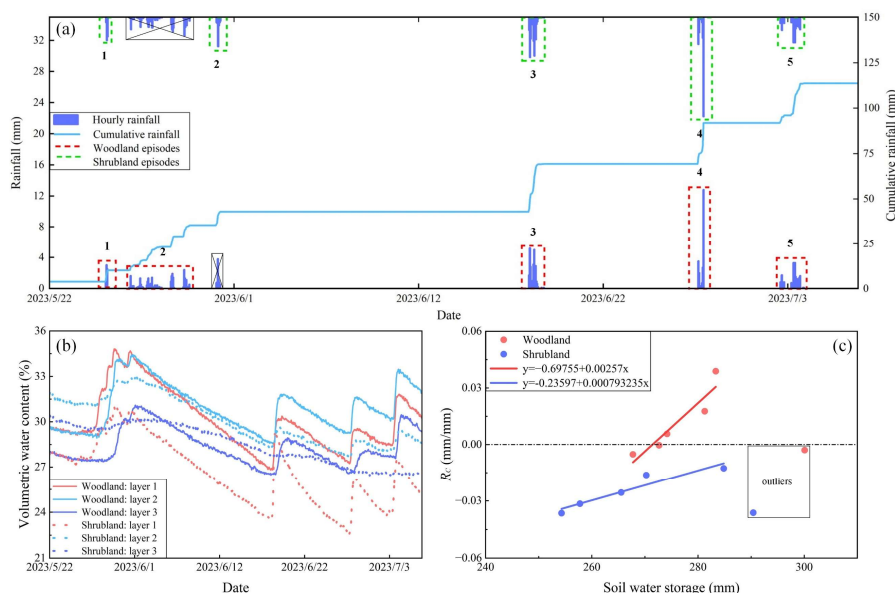
283
 284 **Figure 9.** Schematic dye-stained vertical soil profiles at different hillslope positions. **(a)** Woodland profile; **(b)**
 285 Shrubland profile. Numbers from 0 to 100 denote relative slope positions, with lower values indicating locations
 286 near the slope base.

287 4.3 Slope hydrological characteristics

288 Quantifying how rainfall translates into changes in soil-water content is critical for analyzing rainfall-induced
 289 landslides in this region. To characterize how woodland and shrubland soils respond to rainfall, we group rainfall
 290 events into distinct episodes based on soil depth and in situ saturated hydraulic conductivity (Fig. 10a). Using these
 291 episodes as the basic analytical units, we then assess the intensity of slope-surface responses and the associated water
 292 distribution. This approach overcomes the limitations of using rainfall statistics alone. It explicitly addresses the



293 slope's dynamic absorption-response behavior and shifts the focus from single-storm triggering to a more
 294 comprehensive assessment of cumulative rainfall-response lags.



295
 296 **Figure 10.** Analysis of rainfall, soil moisture, and their coupling from 22 May to 7 July 2023. **(a)** Classification of
 297 rainfall episodes by vegetation type; **(b)** Temporal variation in volumetric soil water content for woodland and
 298 shrubland; **(c)** Coupling between rainfall input and soil moisture response for woodland and shrubland.

299 From 22 May to 7 July 2023, volumetric water content indicates that shrubland soils beneath the sliding layer
 300 (layer 3) are insensitive to rainfall and show only small variations in water content (Fig. 10b). This is consistent with
 301 the findings in Sect. 4.2. In shrubland, most water remains near the surface, and infiltration capacity is low. To
 302 characterize the rainfall-soil-water coupling process, we introduce the index R_c , which quantifies how efficiently
 303 rainfall is converted into soil-water storage (Fig. 10c). A steeper R_c -rainfall regression slope indicates a more
 304 pronounced soil moisture response to rainfall.

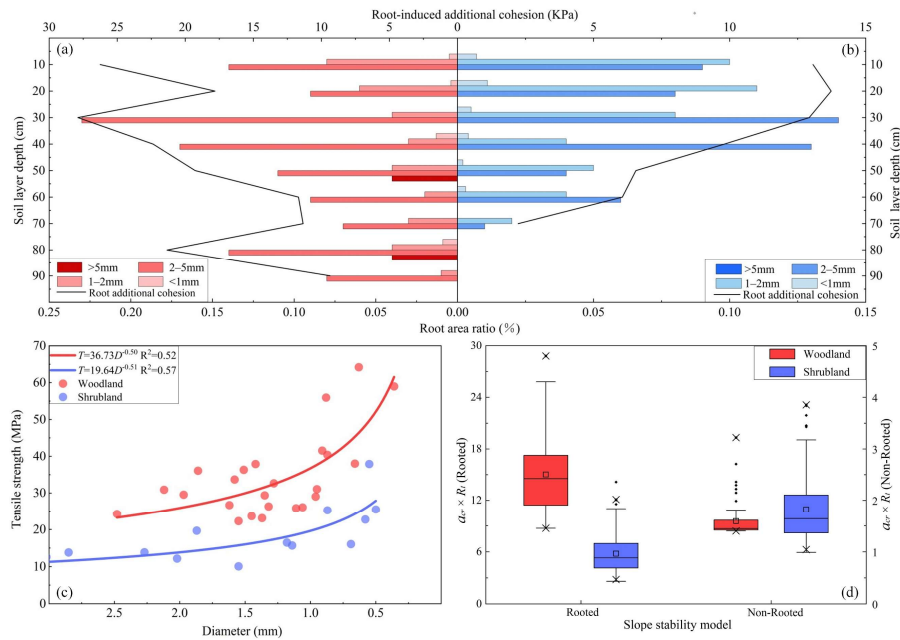
305 In woodland, R_c values are generally positive, indicating that increases in soil-water content often exceed local
 306 rainfall input. Woodland soils have better-developed preferential flow paths than shrubland soils. This suggests that
 307 the observed excess arises because water infiltrating into upslope soils moves downslope as subsurface flow. This
 308 interpretation is consistent with the dye-tracer experiments. In woodland, foot-slope profiles show greater staining
 309 depths than upslope profiles (Fig. 8a). By contrast, early shallow saturation in shrubland diverts part of the rainfall
 310 input into overland flow, reducing conversion efficiency and yielding mostly negative R_c values. Overall, high R_c
 311 values in woodland reflect a strong hydrological response to rainfall and a greater capacity to buffer soil moisture.
 312 In shrubland, a pronounced response lag and low conversion efficiency lead to negative R_c values. These patterns
 313 are consistent with the earlier mechanism-based interpretation.

314 4.4 Effects of vegetation roots on hillslope stability

315 Root spatial distribution and mechanical properties differ markedly between woodland and shrubland soils
 316 (Figs. 11a, 11b, and 11c). Field measurements indicate that maximum rooting depths in woodland and shrubland are
 317 close to their respective mean landslide depths, at 0.84 m in woodland and 0.54 m in shrubland. This consistency
 318 indicates a close relationship between root distribution and landslide depth. Compared with shrubland, roots in



319 woodland mobilize greater root cohesion at a given root diameter and exhibit a larger specific root area. These roots
 320 therefore create a more extensive root-soil contact interface and form a mechanically stronger root-soil composite.



321
 322 **Figure 11.** Mechanical indices of slope stability in woodland and shrubland. **(a)** Root area ratio and root-induced
 323 cohesion in woodland; **(b)** Root area ratio and root-induced cohesion in shrubland; **(c)** Relationship between root
 324 tensile strength and diameter; **(d)** Slope-stability models for woodland and shrubland. The definitions of the whiskers
 325 are given in the caption of Fig. 5.

326 Using the parameters in Table 2, we constructed a slope stability model to evaluate slope resistance to failure
 327 under specified topographic conditions and rainfall inputs. When root-induced cohesion is ignored, mean $a_{cr} \times R_t$
 328 values in woodland and shrubland are similar, indicating that slope stability differs little between them. When root
 329 effects are included, slope stability increases markedly. In woodland, the $a_{cr} \times R_t$ value rises to 15.02,
 330 approximately 338% higher than in shrubland (Fig. 11d). These results indicate that woodland roots contribute much
 331 more to slope stability than roots in shrubland. Woodland roots substantially increase the critical rainfall and
 332 topographic thresholds for landslide initiation and confirm the key role of roots in strengthening slopes and resisting
 333 landslide-triggering factors.

334 **Table 2** Parameters describing the slope stability model

Parameters	Definition	Woodland	Shrubland
ρ_s (kg·m ⁻³)	Dry soil density	1.37	1.41
θ (°)	Slope gradient	31.71–65.27	22.78–67.96
C' (kPa)	Effective cohesion	5.97	7.35
C_r (kPa)		18.59	10.36
φ (°)	Effective friction angle	18.67	14.50
z (m)	Landslide depth	0.84	0.54
K (mm·h ⁻¹)	Hydraulic conductivity	2.10	0.94



335 **5 Discussion**

336 Long-term vegetation restoration policies may result in the dominant soil erosion process shift from traditional
337 wind and water erosion to landslides (Deng et al., 2022; Yang et al., 2024; Du et al., 2025; Liao et al., 2025).
338 Ecological restoration forests not only increase surface cover, but extend their root systems into potential sliding
339 layers, thereby substantially altering slope hydrological processes and mechanical properties, and acting as an
340 important role in landslide initiation (Zhao et al., 2022; Cai et al., 2024; Chen et al., 2024; Lann et al., 2024). In this
341 context, we focused the landslide initiation difference in two representative restoration forests from the hillslope
342 hydrology and failure resistance heterogeneity.

343 The results of SWCC and HCF agree well with the infiltration patterns observed in dye-tracer experiments. In
344 woodland soils, continuous preferential flow channels promote rapid infiltration, substantial downward water
345 migration, and a high capacity for water storage and drainage. Shrubland soils exhibit scattered preferential flow
346 channels, shorter infiltration pathways, pronounced shallow saturation, and a weaker capacity for water
347 redistribution. The stained area ratio and patch distribution further corroborate these differences. Woodland profiles
348 display vertical and continuous stained bands with greater infiltration depths, whereas shrubland profiles show
349 shallow staining. This comparison indicates that variations in root distribution and diameter modify soil pore
350 structure and thereby affect infiltration (Guan et al., 2024; Lann et al., 2024). Woodland soil with coarse roots and
351 higher porosity facilitate deeper infiltration, whereas shrubland soils with shallow root systems provide lower
352 infiltration capacity (Souza et al., 2023; Xiao et al., 2024; Hu et al., 2025). Preferential flow may result in the excess
353 soil water storage over the rainfall depth, and the results from monitoring multiple natural rainfall events between
354 20 May and 6 July 2023 further corroborate the assumption. In shrubland, soil moisture typically exhibits a delayed
355 and attenuated response to rainfall. R_c values are consistently below zero, indicating low rainfall conversion
356 efficiency. Most rainwater does not infiltrate but instead runs off once shallow soils saturate rapidly. In contrast,
357 once rainfall over woodland slopes reaches a certain intensity, R_c values become positive. This pattern suggests that
358 woodland slopes effectively intercept and infiltrate rainfall, sustain deeper water storage, and delay the development
359 of saturation zones. This discrepancy is also evident in the critical $a_{cr} \times R_t$ values. The failure resistance on
360 woodland slopes is higher than shrubland slopes, which may explain the contrasting distribution patterns observed
361 in landslide number and size.

362 Vegetation-based slope protection has long been regarded as a key measure in traditional soil and water
363 conservation, yet multidisciplinary studies have revealed its dual effects (Gyssels et al., 2005; Sidle and Bogaard,
364 2016; Lann et al., 2024). Some herbaceous plants with shallow root systems can promote rapid surface saturation
365 during intense rainfall, thereby enhancing hillslope runoff and rill erosion (Gong et al., 2024). Certain fast-growing
366 tree species with shallow root systems may provide only limited soil reinforcement and thus increase the risk of
367 shallow landslides (Ghestem and Sidle, 2011; Lin et al., 2024). Moreover, excessively thick litter layers can impede
368 infiltration during short-duration storms and accelerate runoff concentration (Zhou et al., 2018; Rajão et al., 2023).
369 These observations indicate that vegetation-based measures are not universally effective for soil erosion control
370 (Löbmann et al., 2020; Lann et al., 2024). Our results further support this understanding. Shallow landslide initiation
371 depends not only on rainfall but also on vegetation type, which modifies coupled hydrological-mechanical processes
372 on slopes. Woodland slopes, with deep root systems and stable preferential flow channels, enhance slope stability,
373 whereas shrubland slopes, limited by shallow root systems, are more prone to rapid surface failure. This finding
374 provides empirical evidence for forest-type allocation in ecologically sensitive areas. It also highlights the need for
375 appropriate vegetation-type selection and matching in regional soil and water conservation.



376 **6 Conclusions**

377 Vegetation recovery in Chinese Loess Plateau may cause the dominant soil erosion process shift from runoff
378 drive to gravitational attraction, while their role on landslide initiation hasn't been addressed. In this work, we
379 addressed the landslide initiation in woodland and shrubland by landslide spatial patterns, hydrological response,
380 and slope failure resistance. Following results can be drawn:

381 1. Landslides in woodland and shrubland exhibit obvious differences in initiation, depth and number. Shrubland
382 has a higher density of small, shallow landslides, whereas woodland has fewer but deeper and larger failures. This
383 contrast reflects a high-initiation-threshold, deep-seated-failure regime in woodland.

384 2. In shrubland, a loose, discontinuous pore system and pronounced hysteresis concentrate moisture in shallow
385 layers, causing rapid shallow saturation and large rainfall losses. In woodland, stable preferential flow paths promote
386 deeper and more efficient moisture migration, as reflected in higher soil water response index values.

387 3. Woodland roots concentrated at 10–25 cm provides greater root cohesion, greater slope failure resistance,
388 and higher slope stability than shrubland roots confined to 0–10 cm depth. Therefore, the sediment production from
389 landslide erosion in Chinese Loess Plateau may differ in various forest types, which deserves further study in future.

390 **Acknowledgments**

391 This research has been supported by the State Key Program of Natural Science of China (grant no. 42130701), and
392 the Natural Science Foundation of China (grant no. 42177309). The authors extend their gratitude to personnel at
393 the Jixian National Ecosystem Research Station of Shanxi Province, Beijing Forestry University, for their help during
394 field investigations.

395 **Code and data availability**

396 The corresponding author, Prof. Chao Ma, is willing to share the raw/processed data upon reasonable request.

397 **Author contributions**

398 **Prof. Ma** conceived the study based on his expertise in shallow landslides and unsaturated soil mechanics, and
399 proposed the concept of hydrological and hydromechanical coupling for analyzing vegetation-related slope
400 instability. Under the guidance of Prof. Ma, **Ruijie Yang** conducted soil hydrology experiments and drafted the
401 manuscript. **Xi Yang and Xinying Wang** assisted with field investigations. **Yan Zang and Liqun Lyu** contributed
402 research progress on shallow landslides and vegetation–slope interactions in the study area.

403 **Competing interests**

404 The authors declare no conflicts of interest.

405 **References**

- 406 An, J., Gao, G., Yuan, C., and Fu, B.: Inter- and intra-event rainfall partitioning dynamics of two typical xerophytic
407 shrubs in the loess plateau of china, *Hydrology and Earth System Sciences Discussions*, 26, 3885–3900,
408 <https://doi.org/10.5194/hess-26-3885-2022>, 2022.
- 409 Bachmair, S., Weiler, M., and Troch, P. A.: Intercomparing hillslope hydrological dynamics: spatio-temporal
410 variability and vegetation cover effects, *Water Resour. Res.*, 48, W5537, <https://doi.org/10.1029/2011WR011196>,
411 2012.
- 412 Bai, R., Wang, X., Li, J., Yang, F., Shangguan, Z., and Deng, L.: The impact of vegetation reconstruction on soil
413 erosion in the loess plateau, *J. Environ. Manage.*, 363, 121382, <https://doi.org/10.1016/j.jenvman.2024.121382>,



- 414 2024.
- 415 Borrelli, P., Robinson, D. A., Panagos, P., Lugato, E., Yang, J. E., Alewell, C., Wuepper, D., Montanarella, L., and
416 Ballabio, C.: Land use and climate change impacts on global soil erosion by water (2015-2070), *Proc. Natl. Acad.*
417 *Sci. U. S. A.*, 117, 21994-22001, <https://doi.org/10.1073/pnas.2001403117>, 2020.
- 418 Cai, L., Wang, F., Lin, Y., Long, Q., Zhao, Y., Han, J., Ge, W., and Chen, H.: Changes in preferential flow caused
419 by root effects in black locust plantations of different stand ages in the semi-arid region of the loess plateau, *J.*
420 *Hydrol.*, 634, 131086, <https://doi.org/10.1016/j.jhydrol.2024.131086>, 2024.
- 421 Chen, M., Yang, X., Zhang, X., Bai, Y., Shao, M., Wei, X., Jia, Y., Wang, Y., Jia, X., Zhu, Y., Zhang, Q., Zhu, X.,
422 and Li, T.: Response of soil water to long-term revegetation, topography, and precipitation on the chinese loess
423 plateau, *Catena*, 236, 107711, <https://doi.org/10.1016/j.catena.2023.107711>, 2024.
- 424 Deng, J., Ma, C., and Zhang, Y.: Shallow landslide characteristics and its response to vegetation by example of july
425 2013, extreme rainstorm, central loess plateau, china, *Bull. Eng. Geol. Environ.*, 81, 100, <https://doi.org/10.1007/s10064-022-02606-1>, 2022.
- 427 Dibiagio, A., Capobianco, V., Oen, A., and Tallaksen, L. M.: State-of-the-art: parametrization of hydrological and
428 mechanical reinforcement effects of vegetation in slope stability models for shallow landslides, *Landslides*, 21,
429 2417-2446, <https://doi.org/10.1007/s10346-024-02300-1>, 2024.
- 430 Du, P., Chen, Y., Zhao, Y., Qu, L., Liu, H., Liu, Z., Xu, J., and Tian, X.: Formation process and depositional
431 characteristics of mudballs in the loess plateau during extreme rainstorms: dual-threshold constraints on material
432 sources and dynamic conditions, *J. Environ. Manage.*, 391, 126590, [https://doi.org/10.1016/j.jenvman.2025.](https://doi.org/10.1016/j.jenvman.2025.126590)
433 126590, 2025.
- 434 Fan, L., Lehmann, P., Zheng, C., and Or, D.: Rainfall intensity temporal patterns affect shallow landslide triggering
435 and hazard evolution, *Geophys. Res. Lett.*, 47, e2019GL085994, [https://doi.org/https://doi.org/10.1029/2019GL](https://doi.org/https://doi.org/10.1029/2019GL085994)
436 085994, 2020.
- 437 Feng, X., Fu, B., Piao, S., Wang, S., Ciais, P., Zeng, Z., Lü, Y., Zeng, Y., Li, Y., Jiang, X., and Wu, B.: Revegetation
438 in china's loess plateau is approaching sustainable water resource limits, *Nat. Clim. Chang.*, 6, 1019-1022,
439 <https://doi.org/10.1038/nclimate3092>, 2016.
- 440 Franklin, S. M., Kravchenko, A. N., Vargas, R., Vasilas, B., Fuhrmann, J. J., and Jin, Y.: The unexplored role of
441 preferential flow in soil carbon dynamics, *Soil Biology and Biochemistry*, 161, 108398, [https://doi.org/10.1016/](https://doi.org/10.1016/j.soilbio.2021.108398)
442 [j.soilbio.2021.108398](https://doi.org/10.1016/j.soilbio.2021.108398), 2021.
- 443 Fu, B., Wang, S., Liu, Y., Liu, J., Liang, W., and Miao, C.: Hydrogeomorphic ecosystem responses to natural and
444 anthropogenic changes in the loess plateau of china, *Annual Review of Earth & Planetary Sciences*, 45, 223-243,
445 <https://doi.org/10.1146/annurev-earth-063016-020552>, 2016.
- 446 Ghestem, M. and Sidle, R.: The influence of plant root systems on subsurface flow: implications for slope stability,
447 *Bioscience*, 61, 869-879, <https://doi.org/10.1525/bio.2011.61.11.6>, 2011.
- 448 Gong, C., Ni, D., Liu, Y., Li, Y., Huang, Q., Tian, Y., and Zhang, H.: Herbaceous vegetation in slope stabilization:
449 a comparative review of mechanisms, advantages, and practical applications, *Sustainability*, 16, 7620,
450 <https://doi.org/10.3390/su16177620>, 2024.
- 451 Gu, C., Mu, X., Gao, P., Zhao, G., Sun, W., Tatarko, J., and Tan, X.: Influence of vegetation restoration on soil
452 physical properties in the loess plateau, china, *J. Soils Sediments*, 19, 716-728, [https://doi.org/10.1007/s11368-](https://doi.org/10.1007/s11368-018-2083-3)
453 018-2083-3, 2019.
- 454 Guan, N., Bi, H., Song, Y., Lu, S., Lin, D., and Han, J.: Vegetation restoration is affecting the characteristics and
455 patterns of infiltration in the loess plateau, *Catena*, 243, 108190, <https://doi.org/10.1016/j.catena.2024.108190>,
456 2024.



- 457 Gyssels, G., Poesen, J., Bochet, E., and Li, Y.: Impact of plant roots on the resistance of soils to erosion by water: a
458 review, *Progress in Physical Geography*, 29, 189-217, <https://doi.org/10.1191/0309133305pp443ra>, 2005.
- 459 Hao, M., Jin, Z., Luo, D., Cao, G., Jiang, C., Han, H., Yang, S., and Zhang, J.: Rainstorm erosion difference and
460 topographical changes induced by heavy rainfall between afforestation and grassland restoration catchments on
461 the chinese loess plateau, *Geomorphology*, 457, 109243, <https://doi.org/10.1016/j.geomorph.2024.109243>, 2024.
- 462 Hu, J., Ren, Y., Tang, M., Zhang, Z., Yang, K., Zhen, Q., and Han, F.: Effects of vegetation restoration on infiltration
463 patterns and preferential flow in semi-arid areas with shallowly buried soft bedrock (pisha sandstone) in china, *J.*
464 *Hydrol.*, 661, 133546, <https://doi.org/10.1016/j.jhydrol.2025.133546>, 2025.
- 465 Lan, H., Zhao, X., Macciotta, R., Peng, J., Li, L., Wu, Y., Zhu, Y., Liu, X., Zhang, N., and Liu, S.: The cyclic
466 expansion and contraction characteristics of a loess slope and implications for slope stability., *Sci. Rep.*, 11, 2250,
467 <https://doi.org/10.1038/s41598-021-81821-4>, 2021.
- 468 Lann, T., Bao, H., Lan, H., Zheng, H., Yan, C., and Peng, J.: Hydro-mechanical effects of vegetation on slope
469 stability: a review, *Sci. Total Environ.*, 926, 171691, <https://doi.org/10.1016/j.scitotenv.2024.171691>, 2024.
- 470 Laycock, W. A., Geological Survey U. S., I. B., New, J. D. O. W., United, S. F. S., and Rutgers, U. (Eds.):
471 Distribution of roots and rhizomes in different soil types in the pine barrens of new jersey, U.S. Geological Survey
472 Professional Paper, Washington, 1967.
- 473 Li, F., Song, X., Tang, C., Liu, C., Yu, J., and Zhang, W.: Tracing infiltration and recharge using stable isotope in
474 taihang mt., North china, *Environmental Geology*, 53, 687-696, <https://doi.org/10.1007/s00254-007-0683-0>, 2007.
- 475 Li, J., Cui, P., and Yin, Y.: Field observation and micro-mechanism of roots-induced preferential flow by infiltration
476 experiment and phase-field method, *J. Hydrol.*, 623, 129756, <https://doi.org/10.1016/j.jhydrol.2023.129756>, 2023.
- 477 Li, P., Pan, Z., Xiao, T., and Wang, J.: Effects of molding water content and compaction degree on the microstructure
478 and permeability of compacted loess, *Acta Geotech.*, 18, 921-936, <https://doi.org/10.1007/s11440-022-01592-8>,
479 2023.
- 480 Li, S., Zheng, C., Lu, T., Zhou, K., Gu, Y., Wang, B., and Lu, Y.: Characteristics and influencing factors of loess
481 terraces' preferential flow under different typical vegetation cover, *Plant Soil*, in press, <https://doi.org/10.1007/s11104-025-07710-1>, 2025.
- 482
- 483 Liang, H., Li, Y., An, X., Liu, J., Pan, N., and Li, Z.: Soil moisture dynamics and its temporal stability under
484 different-aged caragana korshinskii shrubs in the loess hilly region of china, *Water*, 15, 2334, <https://doi.org/10.3390/w15132334>, 2023.
- 485
- 486 Liao, J., Wang, J., Jiao, J., Yan, Z., Li, J., Zhang, Z., Li, M., Xu, Q., Jiang, X., Zhao, W., Ling, Q., Sheng, H., Chen,
487 Y., and Wu, T.: Rusle tends to overestimate soil erosion in revegetated conditions: evidence from long-term runoff
488 plots monitoring on china's loess plateau, *Catena*, 258, 109285, <https://doi.org/10.1016/j.catena.2025.109285>,
489 2025.
- 490 Lin, Y., Jian, W., Wu, Y., Zhu, Z., Wang, H., Dou, H., and Lai, Z.: Effect of tree roots on heavy rainfall-induced
491 shallow landslides, *Geomatics, Natural Hazards and Risk*, 15, 2360002, <https://doi.org/10.1080/19475705.2024.2360002>, 2024.
- 492
- 493 Liu, X., Feng, T., Zhang, Y., Liu, Y., and Wang, P.: Vegetation restoration affects soil hydrological processes in
494 typical natural and planted forests on the loess plateau, *J. Hydrol.*, 650, 132465, <https://doi.org/10.1016/j.jhydrol.2024.132465>, 2025.
- 495
- 496 Löbmann, M. T., Geitner, C., Wellstein, C., and Zerbe, S.: The influence of herbaceous vegetation on slope stability
497 – a review, *Earth-Sci. Rev.*, 209, 103328, <https://doi.org/10.1016/j.earscirev.2020.103328>, 2020.
- 498 Lu, N. and Godt, J. W. (Eds.): Hillslope hydrology and stability, Cambridge University Press, Cambridge, U.K.,
499 2013.



- 500 Lu, N., Calderon, A. R. A., Wayllace, A., Lovekin, J., and Crandall, A.: Suction stress–based rainfall intensity–
501 duration method for slope instability prediction, *J. Geotech. Geoenviron. Eng.*, 150, 4024069, <https://doi.org/10.1061/JGGEFK.GTENG-12597>, 2024.
- 502
- 503 Masi, E. B., Tofani, V., Rossi, G., Cuomo, S., Wu, W., Salciarini, D., Caporali, E., and Catani, F.: Effects of roots
504 cohesion on regional distributed slope stability modelling, *Catena*, 222, 106853, <https://doi.org/10.1016/j.catena.2022.106853>, 2023.
- 505
- 506 Montgomery, D. R. and Dietrich, W. E.: A physically based model for the topographic control on shallow landsliding,
507 *Water Resour. Res.*, 30, 1153-1171, <https://doi.org/10.1029/93WR02979>, 1994.
- 508 Montgomery, D. R. and Dietrich, W. E.: Landscape dissection and drainage area-slope thresholds, in: *Process*
509 *Models and Theoretical Geomorphology*, edited, John Wiley & Sons, Chichester, 221-246, 1994.
- 510 Montgomery, D. R., Schmidt, K. M., Greenberg, H. M., and Dietrich, W. E.: Forest clearing and regional landsliding,
511 *Geology*, 28, 311-314, [https://doi.org/10.1130/0091-7613\(2000\)28<311:FCARL>2.0.CO;2](https://doi.org/10.1130/0091-7613(2000)28<311:FCARL>2.0.CO;2), 2000.
- 512 Nimmo, J. R., Perkins, K. S., Schmidt, K. M., Miller, D. M., Stock, J. D., and Singha, K.: Hydrologic characterization
513 of desert soils with varying degrees of pedogenesis: 1. Field experiments evaluating plant-relevant soil water
514 behavior, *Vadose Zone J.*, 8, 480-495, <https://doi.org/10.2136/vzj2008.0052>, 2009.
- 515 Niu, F., Pan, C., and Cui, Y.: Experimental investigation to the effect of different land-use on rainfall infiltration
516 runoff patterns and preferential flow distribution in the loess area of western shanxi province, *Acta Ecologica*
517 *Sinica*, 43, 4144-4166, <https://doi.org/10.5846/stxb202204130989>, 2023.
- 518 Rajão, P., Berg, M., Cornelissen, J., and Dias, A.: The effects of leaf traits on litter rainfall interception with
519 consequences for runoff and soil conservation, *J. Ecol.*, 111, 2662-2675, <https://doi.org/10.1111/1365-2745.14203>,
520 2023.
- 521 Schwarz, M., Preti, F., Giadrossich, F., Lehmann, P., and Or, D.: Quantifying the role of vegetation in slope stability:
522 a case study in tuscany (italy), *Ecol. Eng.*, 36, 285-291, <https://doi.org/10.1016/j.ecoleng.2009.06.014>, 2010.
- 523 Sidle, R. C. and Bogaard, T. A.: Dynamic earth system and ecological controls of rainfall-initiated landslides, *Earth-*
524 *Sci. Rev.*, 159, 275-291, <https://doi.org/10.1016/j.earscirev.2016.05.013>, 2016.
- 525 Souza, L. F. T., Hirmas, D. R., Sullivan, P. L., Reuman, D. C., Kirk, M. F., Li, L., Ajami, H., Wen, H., Sarto, M. V.
526 M., Loecke, T. D., Rudick, A. K., Rice, C. W., and Billings, S. A.: Root distributions, precipitation, and soil
527 structure converge to govern soil organic carbon depth distributions, *Geoderma*, 437, 116569,
528 <https://doi.org/10.1016/j.geoderma.2023.116569>, 2023.
- 529 Tang, B., Jiao, J., Zhang, Y., Chen, Y., Wang, N., and Bai, L.: The magnitude of soil erosion on hillslopes with
530 different land use patterns under an extreme rainstorm on the northern loess plateau, china, *Soil and Tillage*
531 *Research*, 204, 104716, <https://doi.org/10.1016/j.still.2020.104716>, 2020.
- 532 Tang, P., Zhang, J., Li, Y., Wei, G., Hu, Y., and Zhao, J.: Effects of extreme rainfall on the morphological
533 characteristics and spatial distribution of shallow landslides under different land use patterns in the loess region of
534 western shanxi province, northern china, *Journal of Beijing Forestry University*, 45, 109-117, <https://doi.org/10.12171/j.1000-1522.20230070>, 2023.
- 535
- 536 Wang, N. and Zhang, T.: Soil pore structure and its research methods: a review, *Soil Water Res.*, 19, 1-24,
537 <https://doi.org/10.17221/64/2023-SWR>, 2024.
- 538 Wang, R., Dong, Z., Zhou, Z., Wang, N., Xue, Z., and Cao, L.: Effect of vegetation patchiness on the subsurface
539 water distribution in abandoned farmland of the loess plateau, china, *Sci. Total Environ.*, 746, 141416,
540 <https://doi.org/10.1016/j.scitotenv.2020.141416>, 2020.
- 541 Wang, R., Dong, Z., Zhou, Z., and Wang, P.: Temporal variation in preferential water flow during natural vegetation
542 restoration on abandoned farmland in the loess plateau of china, *Land*, 8, 186, <https://doi.org/>



- 543 10.3390/land8120186, 2019.
- 544 Wang, X., Ma, C., Lyu, L., and Zhang, Y.: Erosion characteristics of shallow landslides under various land-use
545 conditions: an example of the caijiachuan landslide, *Arid Zone Research*, 41, 697-705,
546 <https://doi.org/10.13866/j.azr.2024.04.15>, 2024.
- 547 Wang, Y., Dong, G., Qu, L., Wu, Z., Zhao, F., and Shao, C.: Ecosystem functioning of the loess plateau in china
548 from vegetation restoration relied largely on climate, *Forests*, 14, 27, <https://doi.org/10.3390/f14010027>, 2022.
- 549 Wei, Y. Z., Yao, Z. H., Chong, X. L., Zhang, J. H., and Zhang, J.: Microstructure of unsaturated loess and its
550 influence on strength characteristics, *Sci. Rep.*, 12, 1502, <https://doi.org/10.1038/s41598-022-05464-9>, 2022.
- 551 Wen, S., Shao, M., and Wang, J.: Earthworm burrowing activity and its effects on soil hydraulic properties under
552 different soil moisture conditions from the loess plateau, china, *Sustainability*, 12, 9303, <https://doi.org/10.3390/su12219303>, 2020.
- 554 Xiao, T., Li, P., Fei, W., and Wang, J.: Effects of vegetation roots on the structure and hydraulic properties of soils:
555 a perspective review, *Sci. Total Environ.*, 906, 167524, <https://doi.org/10.1016/j.scitotenv.2023.167524>, 2024.
- 556 Xu, P., Zhang, Q., Qian, H., Li, M., and Yang, F.: An investigation into the relationship between saturated
557 permeability and microstructure of remolded loess: a case study from chinese loess plateau, *Geoderma*, 382,
558 114774, <https://doi.org/10.1016/j.geoderma.2020.114774>, 2021.
- 559 Yamase, K., Ikeno, H., Hotta, N., Imawaka, M., Ohashi, M., Tanikawa, T., Todo, C., Dannoura, M., and Hirano, Y.:
560 Effect of sprouting and corresponding root distribution of the shrub species *eurya japonica* on slope stability,
561 *Catena*, 238, 107869, <https://doi.org/10.1016/j.catena.2024.107869>, 2024.
- 562 Yan, X., Nunes, J. P., Sun, J., Tang, D., Wen, Y., and Li, Z.: Restored vegetation dominates the decrease in surface
563 and subsurface runoff on the loess plateau, *J. Hydrol.*, 640, 131730, <https://doi.org/10.1016/j.jhydrol.2024.131730>,
564 2024.
- 565 Yang, B., Jiao, J., Ma, X., Zhao, W., Ling, Q., Zhang, X., Han, J., Du, P., Chen, Y., and Chen, H.: Distribution and
566 formation of soil balls under heavy rainstorm conditions in the northern loess plateau, *J. Hydrol.*, 625, 130103,
567 <https://doi.org/10.1016/j.jhydrol.2023.130103>, 2023.
- 568 Yang, B., Ma, X., Jiao, J., Zhao, W., Ling, Q., Li, J., and Zhang, X.: Magnitude and hotspots of soil erosion types
569 during heavy rainstorm events on the loess plateau: implications for watershed management, *Catena*, 246, 108365,
570 <https://doi.org/10.1016/j.catena.2024.108365>, 2024.
- 571 Zhang, S., Liu, Y., Yang, M., Tian, P., Mu, X., and Zhao, G.: Impact of vegetation restoration on preferential flow
572 and soil infiltration capacity in the hilly region of the loess plateau, *Journal of Hydrology: Regional Studies*, 59,
573 102333, <https://doi.org/10.1016/j.ejrh.2025.102333>, 2025.
- 574 Zhang, Y., Tang, Z., Zhang, J., Zhang, Z., and Zhang, M.: Visualizing preferential flow paths using dye tracer and
575 species diversity theory methods to explore their correlation to soil properties with random forest algorithm, *J.*
576 *Hydrol.*, 638, 131570, <https://doi.org/10.1016/j.jhydrol.2024.131570>, 2024.
- 577 Zhao, M., Li, D., Huang, Y., Deng, Y., Yang, G., Lei, T., and Huang, Y.: Soil matrix infiltration characteristics in
578 differently aged eucalyptus plantations in a southern subtropical area in china, *Catena*, 217, 106490,
579 <https://doi.org/10.1016/j.catena.2022.106490>, 2022.
- 580 Zhou, Q., Zhou, X., Luo, Y., and Cai, M.: The effects of litter layer and topsoil on surface runoff during simulated
581 rainfall in guizhou province, china: a plot scale case study, *Water*, 10, 915, <https://doi.org/10.3390/w10070915>,
582 2018.
- 583